Competitive actions of MnSi in the epitaxial growth of Mn5Si3 thin films on Si(111)

Ismaïla Kounta, Helena Reichlova, Dominik Kriegner, Rafael Lopes Seeger, Antonin Bad'Ura, Miina Leiviska, Amine Boussadi, Vasile Heresanu, Sylvain Bertaina, Matthieu Petit, et al.

Competitive actions of MnSi in the epitaxial growth of Mn_5Si_3 thin films on Si(111)

Ismaïla Kounta,[1] Helena Reichlova,[2,3] Dominik Kriegner,[2,3] Rafael Lopes Seeger,[4] Antonin Bad'ura,[3,5] Miina Leiviska,[4] Amine Boussadi,[1] Vasile Heresanu,[1] Sylvain Bertaina,[6] Matthieu Petit,[1] Eva Schmoranzerova,[5] Libor Smejkal,[3,7] Jairo Sinova,[3,7] Tomas Jungwirth,[3,8] Vincent Baltz,[4] Sebastian T. B. Goennenwein,[9] and Lisa Michez[1,*]

[1]*Aix Marseille Univ, CNRS, CINAM, AMUTECH, Marseille, France*

[2]*Institut für Festkörper- und Materialphysik and Würzburg-Dresden Cluster of Excellence ct.qmat, Technische Universität Dresden, 01062 Dresden, Germany*

[3]*Institute of Physics, Czech Academy of Sciences, Cukrovarnická 10, 162 00 Praha 6, Czech Republic*

[4]*University of Grenoble Alpes, CNRS, CEA, Grenoble INP, Spintec, F-38000 Grenoble, France*

[5]*Department of Chemical Physics and Optics, Faculty of Mathematics and Physics, Charles University, Ke Karlovu 3, 121, 16 Praha 2, Czech Republic*

[6]*Aix Marseille Univ, CNRS, IM2NP, Marseille, France*

[7]*Institut für Physik, Johannes Gutenberg Universität Mainz, 55128 Mainz, Germany*

[8]*School of Physics and Astronomy, University of Nottingham, NG7 2RD Nottingham, United Kingdom*

[9]*Universität Konstanz, Fachbereich Physik, 78457 Konstanz, Germany*

(Received 8 October 2022; accepted 26 January 2023; published 23 February 2023)

Some magnetically ordered phases of the Mn_5Si_3 crystal are proving to be prototypes for the study of the new fundamental spin physics related to the spontaneous breaking of the time-reversal symmetry despite a zero net magnetization. Here, we report on a route to grow epitaxial Mn_5Si_3 thin films on Si(111). To this end, we use Mn and Si codeposition in a molecular beam epitaxy system and carefully tune the deposition rates, the growth temperature, and the annealing temperature. We assessed the silicide phase-formation and morphology using reflection high-energy electron diffraction, x-ray diffraction, high-resolution transmission electron microscopy (HRTEM) and atomic force microscopy. Layers containing only Mn_5Si_3 could be stabilized under very restrictive conditions, by tuning the Mn/Si flux ratio to match the compound stoichiometry and adjusting the substrate temperature during growth to 443 K. HRTEM imaging revealed the existence of an interfacial amorphous layer of few nanometers thickness. Annealing the heterostructure up to 573 K led to the formation of MnSi at the vicinity of the Mn_5Si_3/Si(111) interface, which significantly reduced the nucleation barrier of Mn_5Si_3. High-quality crystalline Mn_5Si_3 thin films were then formed with the following epitaxial relationships: $Mn_5Si_3(0001)[01\bar{1}0]//MnSi(111)[\bar{2}11]//Si(111)[1\bar{1}0]$. Our experiments showed that the formation of MnSi is enhanced at a growth temperature above 473 K or for a longer annealing step, while the crystalline quality of the Mn_5Si_3 overlayer is correspondingly degraded leading to textured thin films. The growth pathways and structural properties of the manganese silicides can be rationalized in terms of reactions maximizing the free-energy lowering rate. Moreover, we found that the magnetic and the magnetotransport properties can be used as an efficient tool to track both Mn_5Si_3 crystallinity and proportion in the deposited layers.

DOI: 10.1103/PhysRevMaterials.7.024416

I. INTRODUCTION

Silicon- and manganese-based systems attract a great deal of attention due to their high compatibility with the mainstream technologies, the abundance of these elements in the Earth's crust, and most importantly, the fascinating properties exhibited by Mn-Si alloys. Whereas the higher manganese silicides ($MnSi_{2-x}$ with $x = 0.25$–0.27) are promising for thermoelectric applications [1], the other compounds display a wide variety of exotic magnetic structures very interesting for spintronics. As an example, the well-studied manganese monosilicide (MnSi) is a weak itinerant ferromagnet. Its lack of a symmetry center leads to a ferromagnetic spiral in the ordered phase along the [111] direction which can host skyrmions [2,3]. In contrast, complex antiferromagnetic (AF) arrangements were evidenced in Mn_3Si and Mn_5Si_3. Whereas the first compound develops incommensurate antiferromagnetic order [4,5], Mn_5Si_3 displays a complex modulated magnetic structure, which in bulk is known to give rise to two first-order transitions from a noncollinear antiferromagnetic structure (AF1) at low temperatures, to a collinear antiferromagnetic high-temperature phase structure (AF2) at 66 K, and from the latter to paramagnetism (PM) at 99 K [6–9]. In addition to this rich temperature- and field-dependent spin structure [10], ferromagnetic order was evidenced in the isostructural C-doped $Mn_5Si_3C_x$ up to 350 K [11,12]. A similar doping effect was observed in isostructural $Mn_5Ge_3C_x$ for which the Curie temperature is boosted from 296 K in the undoped compound up to 450 K [13,14].

Materials with spontaneous symmetry breaking can display various kinds of intriguing phenomena such as the

*lise.michez@univ-amu.fr

anomalous Hall effect in itinerant magnets and the topological Hall effect (THE) in materials with nontrivial spin structures. These effects were observed in ferromagnetic $Mn_5Si_3C_x$ [15] and in the Mn_5Si_3 noncollinear AF phase [16], respectively. In addition, a novel-type of anomalous Hall effect has been discovered in monocrystalline Mn_5Si_3 thin films in its collinear AF arrangement [17] and it is discussed in the context of altermagnetic spin and crystal symmetry [19]. Mn_5Si_3 appears therefore as a material for the investigation of fundamental new spin physics related to time reversal symmetry breaking in the band structure [18–25].

The integration of thin films and nanomaterials on common semiconductor substrates such as silicon is a crucial prerequisite for future applications. Crystalline films are essential for revealing intrinsic materials properties, such as the anomalous Hall effect arising from the altermagnetic phase [20]. The signature of this novel phenomenon was discovered in epitaxial Mn_5Si_3 thin films [17], while it was not observed in polycrystalline layers [16] or bulk samples [10]. However, in the epitaxial heterostructure, the formation of a undesired MnSi was observed at the interface Mn_5Si_3 /Si(111). There is no report to date on the formation of a sole Mn_5Si_3 thin film directly grown in epitaxy on Si(111). Previous studies addressing the growth of manganese silicides were performed either by solid phase epitaxy (SPE) [26–28] or reactive phase epitaxy (RDE) [29,30], where a Mn layer was deposited on the silicon substrate at room temperature or at higher temperature, respectively. An annealing step commonly completed the film fabrication. The Si atoms required to form the manganese silicides originated from the Si substrate. Such procedures usually led to the formation of many different polycrystalline Mn–silicide phases [27,28,30] and/or to a rough surface due to the islanding during the growth process [31,32]. A moderate annealing step with a substrate temperature of ∼673 K systematically led to the formation of the MnSi phase [28]. An alternative technique is the codeposition of Mn and Si on the Si substrate, either simultaneously [33] or by alternating atomic-layer deposition [34]. With this process, only a mild annealing of the deposited layer is subsequently required to form the desired compound. This technique was successfully applied for the realization of MnSi smooth films [33] and of very high-quality Mn_5Ge_3/Ge(111) heterostructures [35].

The present study aimed at investigating the growth of manganese silicides on Si(111) substrates using the codeposition technique with the objective of stabilizing a sole monocrystalline Mn_5Si_3 thin film with a thickness in the range of 15–25 nm. The threefold symmetry of the Si(111) substrate surface orientation is prone to the stabilization of the hexagonal Mn_5Si_3 phase as already observed in the isostructural Mn_5Ge_3 compound grown on Ge(111) [36]. Here we combined reflection high-energy electron diffraction (RHEED), x-ray diffraction (XRD), transmission electron microscopy (TEM), and atomic force microscopy (AFM) experiments to determine the nature and structure of the phases present in the thin films, their epitaxial relationships with the substrate and their roughness as a function of the growth conditions. We evidenced a narrow window of growth parameters allowing to stabilize Mn_5Si_3 thin films, using growth rates in the range of 2–4 Å min^{-1}. High crystallinity is only achieved when a thin MnSi layer is present at the interface. This undesired MnSi phase could be suppressed at the expense of crystalline quality. The formation of different phases and their structural properties can be consistently understood in terms of reactions maximizing the free-energy lowering rate. We found that the different silicide phases within the films can be tracked via magnetization measurements. We finally evidenced an interplay between structural and transport properties: the magnitude of the spontaneous Hall effect measured in its AF2 arrangement [17] directly depends on the Mn_5Si_3 phase proportion and its degree of crystallinity.

II. EXPERIMENTS DETAILS

Thin films of Mn_5Si_3 were grown by codeposition of manganese and silicon on Si(111) substrates using molecular beam epitaxy (MBE) with a base pressure below 10^{-10} Torr. Prior to the growth, the Si(111) substrates were chemically cleaned using the modified Shiraki method [37] to remove surface impurities and create a thin and smooth protective oxide layer. The latter was then thermally removed *in situ* by annealing up to 1173 K. Subsequently, a 10-nm-thick intrinsic Si buffer layer was grown at 873 K and annealed at 973 K to provide a high-quality starting surface for the silicide growth with a well-developed Si(111)-(7 × 7) reconstruction. Mn and Si were evaporated from a standard Knudsen effusion cell and a Si sublimation source from MBE-Komponenten, respectively. The deposition rates were carefully calibrated using a quartz balance. The pressure during growth did not exceed 10^{-9} Torr. A post-annealing step was often required to improve the crystal quality, especially for codeposition at substrate temperature lower than 473 K. Growth parameters such as the substrate temperature during growth and annealing as well as Mn and Si fluxes were found critical for the silicide phase formation and their crystallinity. In this study, we focus on samples with film thicknesses between 13 and 27 nm.

Substrate surface condition and crystal structure of the film surface was monitored *in situ* using RHEED. A subsequent structural analysis of the films was performed by XRD to determine the structure and orientation of the films and identify the nature of phases formed during the growth. The measurements were realized using a high brilliancy rotating anode Rigaku RU-200BH, equipped with an image plate detector Mar345 and operating with the nonmonochromatic Cu K_α radiation. The experimental resolution is about 0.3° in 2θ. The films thickness and the interface quality were probed by x-ray reflectivity (XRR) using a Panalytical X'Pert PRO diffractometer and nonmonochromatic Cu K_α radiation. The surface topographies were imaged by AFM over an area of 5 × 5 μ m^2 with a Nanoscope IIIA Multimode from Digital instruments. The quality of the interface and the epitaxial relationships of the samples were confirmed by TEM on a Jeol 3010 microscope operating at 300 kV with a spatial resolution of 1.7 Å. The cross-sectional TEM samples were prepared using a focused dual ion beam (FEI Helios 600 NanoLab). All structural measurements have been performed at 300 K in the Mn_5Si_3 hexagonal phase [7].

DC magnetic susceptibility measurements were performed using a conventional MPMS-XL SQUID magnetometer from Quantum Design operating at a magnetic field up to 5 T and temperature down to 2 K. In the magnetometry data discussed

below, the diamagnetic contribution due to the silicon substrate was subtracted, by removing the signal of an identical bare Si substrate. Field-cooled curves were recorded under an applied magnetic field of 100 Oe. Hysteresis ($M - H$) curves have been measured for various temperatures in the 2–300 K range. Measurements with both in-plane and out-of-plane magnetic fields were performed.

The MBE grown films were lithographically patterned into Hall bar microstructures for the magnetotransport experiments. Standard optical lithography was used, followed by Ar plasma etching. The magnetotransport experiments were done in either a vector magnet cryostat system from Oxford Instruments equipped with a variable temperature insert or in a Quantum Design PPMS system. A typical current density of 3×10^5 A/cm^2 was used and transversal voltages were measured using the so-called Delta method [38]. In the data shown below, the measured transversal voltage was antisymmetrized with respect to the magnetic field to isolate the Hall effect contribution.

III. STRUCTURAL PROPERTIES AND PHASE FORMATION

A. Composition and structures of Mn silicide thin films

The composition and structure of the manganese silicide thin films were investigated with regard to growth temperatures (T_G), deposition rates, and post-deposition annealing temperature *in situ* (T_A). A series of manganese silicides films was grown by MBE on atomically flat Si(111). The RHEED patterns of the initial Si surface exhibited a well-defined (7 × 7)-reconstruction with Kikuchi lines indicating a high-quality starting surface as shown in Figs. 1(a) and 1(d). The Si deposition rate (V_{Si}) was fixed at 2 Å min^{-1} and the Mn rate (V_{Mn}) was varied between 2 and 4 Å min^{-1} to sweep over the stoichiometry of Mn_5Si_3. Epitaxial growth is performed by opening both Mn and Si shutters simultaneously. The Mn/Si flux ratio $R_{Mn/Si}$ was then defined as $\frac{V_{Mn}}{V_{Si}}$. For each $R_{Mn/Si}$ value, the experiments were conducted with substrates maintained at a fixed temperature during deposition (T_G) in the range of 300 to 673 K. The samples were further annealed *in situ*, if required, until the appearance of a well-defined RHEED pattern. The highest annealing temperature was 723 K to prevent the formation of a single MnSi phase. A typical $(\sqrt{3} \times \sqrt{3})$R30° surface reconstruction is observed in every silicides films as shown in Figs. 1(b), 1(c), 1(e), and 1(f). However, a careful measurement of the spacing between streaks revealed the presence of two distinct phases (i.e., MnSi and Mn_5Si_3) depending on the growth conditions. In addition, the intensity modulation of the streaks presented characteristic differences that will be discussed in the following sections.

Beside this surface-sensitive characterization, a complete analysis of the crystal structure over the whole film thickness was performed using XRD. Two-dimensional diffraction (2D-XRD) maps were recorded for manganese silicide films fabricated under different growth conditions. Figures 2(a), 2(c), and 2(e) show three representative diffraction patterns of characteristic samples dubbed S1, S4, and S5, respectively. The growth parameters used for these films are indicated in Fig. 4. The angle between the incident x-ray beam and the sample surface along the Si(111)-[1$\bar{1}$0] varied from 16 to 20°

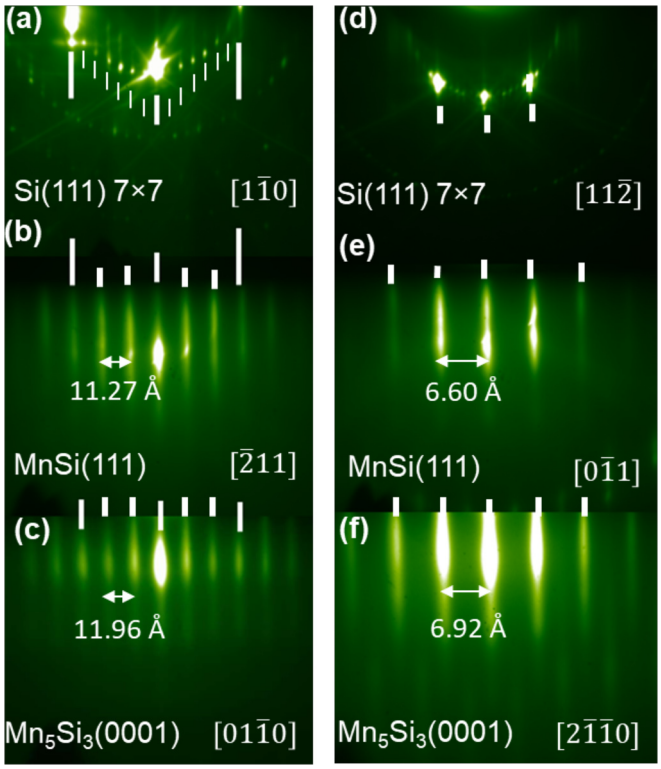

FIG. 1. RHEED patterns taken along the Si(111)-[1$\bar{1}$0] [(a)–(c)] and Si(111)-[11$\bar{2}$] [(d)–(f)] azimuths with an incident electron energy of 30 keV. The bulk (1 × 1) streaks are indicated by large white rods and reconstructed streaks by smaller rods; [(a), (d)] RHEED patterns of the Si(111) (7 × 7) surface prior to the Mn and Si codeposition; [(b), (e)] RHEED patterns observed after codeposition of ∼20-nm-thick film of Mn and Si at 573 K and a short annealing up to 623 K. A typical $(\sqrt{3} \times \sqrt{3})$R30° surface reconstruction is observed with a spacing between the RHEED streaks corresponding to 11.27 Å and 6.60 Å in the MnSi(111)-[$\bar{2}$11] and [0$\bar{1}$1], respectively. [(c), (f)] A similar $(\sqrt{3} \times \sqrt{3})$R30° reconstruction is obtained after a codeposition of Mn and Si at 443 K and a short annealing up to 623 K. The sample thickness is ∼20 nm. The distances extracted from the streak spacing (11.96 Å and 6.92 Å for Mn_5Si_3 (0001)-[01$\bar{1}$0] and [2$\bar{1}\bar{1}$0] azimuths, respectively) are characteristic of the Mn_5Si_3 phase.

during the acquisition, which covers the main Bragg peaks of the Mn silicides. The plots of the respective integrated intensities for an equal radial distance in the 2D patterns (which corresponds to an equal 2θ angle), are shown in Figs. 2(b), 2(d), and 2(f). Although the Si(111) crystal was not in Bragg diffraction conditions in the selected angular range, two broad and attenuated signals coming from the substrate are noticeable around $2\theta = 28.4°$ and $2\theta = 47.3°$. We assign these features to thermal diffuse scattering at the Si(111) and Si(220) Bragg positions, respectively. The 2D-XRD images exhibited spots or small circular arcs that could all be satisfactorily identified using the reflections of both MnSi and Mn_5Si_3 compounds. Mn_5Si_3 crystallizes in the hexagonal $P6_3/mcm$ structure ($a = 6.910$ Å and $c = 4.814$ Å in bulk crystals [39]), while the face-centered cubic MnSi belongs to $P2_13$ space group with a bulk lattice parameter of 4.548 Å [40]. For the sake of clarity, the crystal structures of Si, MnSi, and Mn_5Si_3 are illustrated in Figs. 3(a), 3(b),

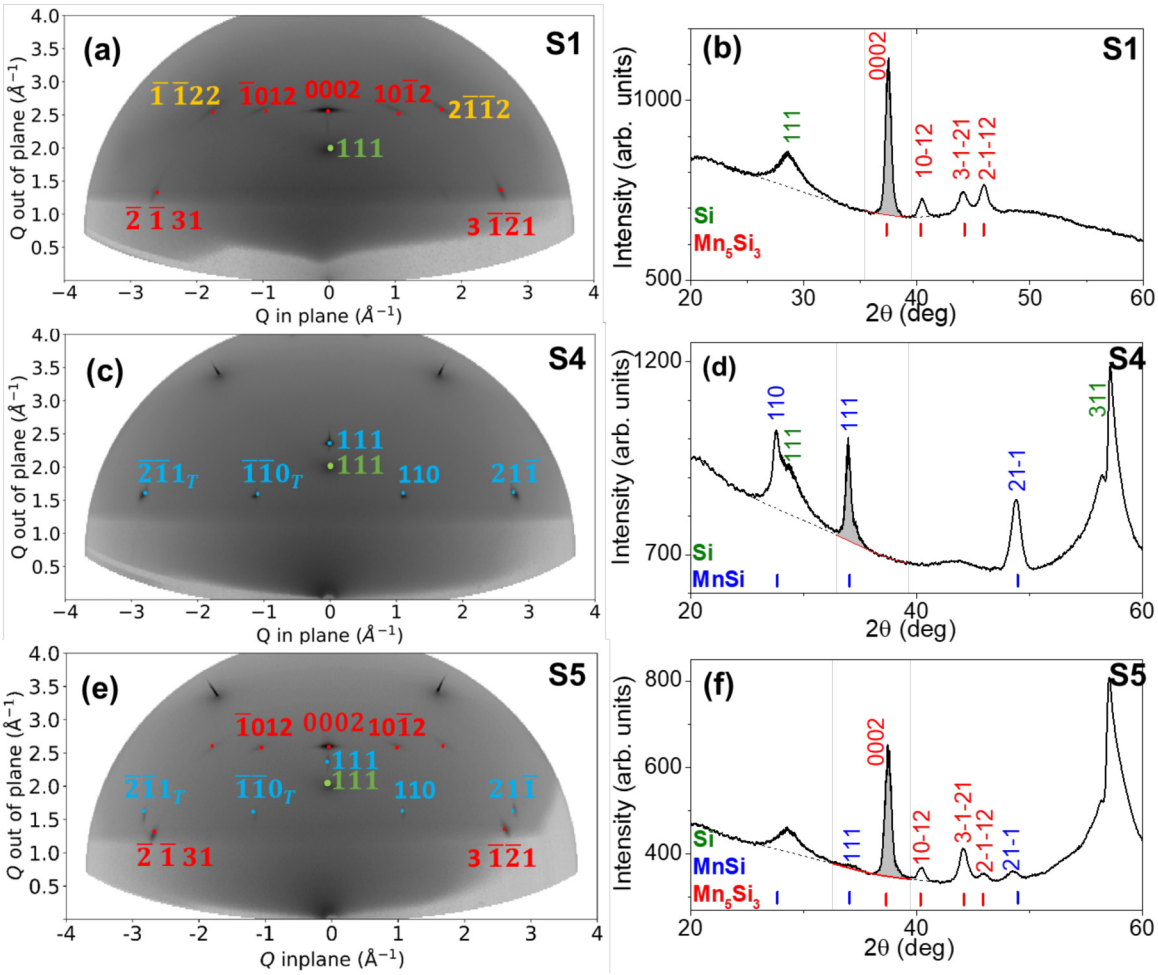

FIG. 2. [(a), (c), (e)] 2D-XRD pattern of films of Mn_5Si_3 (*S*1 sample), MnSi (*S*4 sample) and a mixture of the two phases (*S*5 sample), respectively. [(b), (d), (f)] Plots of the integrated intensities for an equal radial distance, i.e., an equal 2θ angle, of the diffraction images shown in panels [(a), (c), (e)], respectively. The intensity is normalized by the number of contributing pixels, producing the equivalent of 2θ scans.

and 3(c), respectively whereas the local positions of Si and Mn atoms along the growth direction are shown in Figs. 3(d), 3(e), and 3(f). The yellow planes indicate the planes parallel to the surface, i.e., perpendicular to the growth direction. The MnSi epilayer is known to adopt a 30° rotation about the growth direction with respect to the Si(111) substrate to reduce lattice mismatch [41], giving the following epitaxial orientation for MnSi and Mn_5Si_3 with respect to Si(111): $Mn_5Si_3(0001)[01\bar{1}0]//MnSi(111)[\bar{2}11]//Si(111)[1\bar{1}0]$. The Bragg positions and corresponding indexes are shown in Fig. 2 with blue and red marks for MnSi and Mn_5Si_3, respectively. For MnSi Bragg reflections, a "T" denotes reflections from the film volume with enantiomorphic twins introduced by the achiral Si(111) structure [29,30,42,43]. Their similar intensities indicate the same volume fractions for both domain types. No other phases could be detected in the investigated range of growth parameters. The absence of Debye rings is consistent with an epitaxial growth although a small mosaicity is present in the samples containing only Mn_5Si_3. Detailed structural analysis for each phase will be presented in the following section.

The acquired XRD curves correspond therefore to the diffraction pattern of Mn_5Si_3 [Figs. 2(a) and 2(b)], MnSi [Figs. 2(c) and 2(d)] or a superposition of the two patterns [Figs. 2(e) and 2(f)]. To assess the thin films composition, we considered the brightest reflection of each phase, i.e., the nonoverlapping (111) and (0002) Bragg reflections of MnSi and Mn_5Si_3, respectively. This corresponds to diffraction from planes parallel to the surface. The peaks were fitted using Gaussian curves to find the peak parameters such as maximum intensity, area, full width at half maximum (FWHM) and position. The relative fraction of Mn_5Si_3 ($C_{Mn_5Si_3}$) and MnSi (C_{MnSi}) in the film was determined from the background-subtracted x-ray intensities of Mn_5Si_3 and MnSi Bragg peaks and considering their respective structure factor [44]. To relate the growth conditions to the phase formation, we plotted the respective concentrations of Mn_5Si_3 and MnSi as a function of T_G and $R_{Mn/Si}$ for a given T_A of 573 K [Fig. 4(a)]. The suitable conditions for the preponderant formation of the Mn_5Si_3 phase were found for a narrow set of growth parameters corresponding to $R_{Mn/Si} \approx 1.6$, $T_G \approx 443$ K. Slight deviation from these conditions led to the appearance of MnSi phase that predominantly developed at the expense of Mn_5Si_3, eventually resulting in a film only consisting of MnSi. The effect of T_A was then investigated for the values of $R_{Mn/Si}$ and T_G leading to the highest concentration in Mn_5Si_3, as illustrated

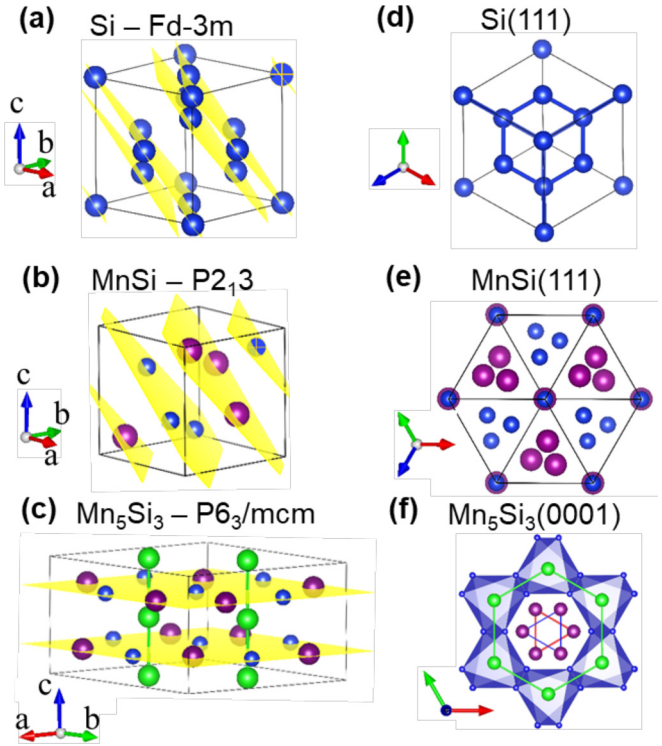

FIG. 3. [(a)–(c)] Crystal structures of Si, MnSi, and Mn_5Si_3, respectively. The blue and purple circles indicate the positions of the Si and Mn atoms, respectively. The green dots in the Mn_5Si_3 cell represent also Mn atoms that are in nonequivalent positions. The yellow planes indicate the planes perpendicular to the growth direction. [(d), (e), (f)] Schematic representations of Si, MnSi and Mn_5Si_3 structures along the growth direction (i.e., (111) for Si and MnSi, and (0001) for Mn_5Si_3).

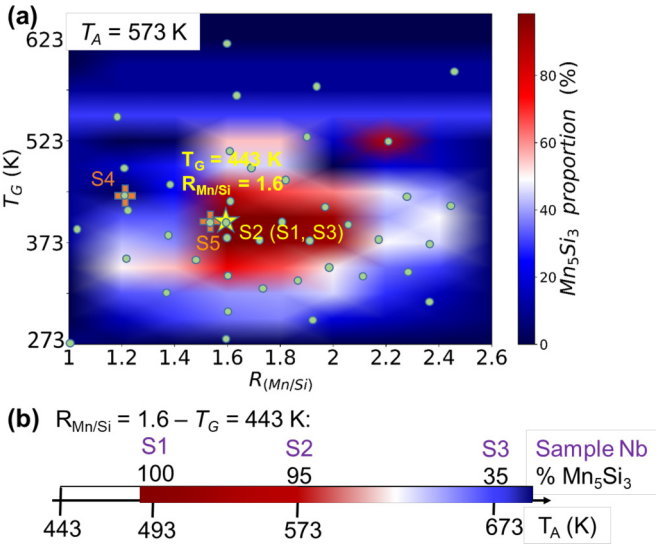

FIG. 4. (a) Mn_5Si_3 proportion within the thin film as a function of the substrate temperature during growth and the Mn/Si flux ratio ($R_{Mn/Si}$) for the same annealing conditions (except for samples *S*1 and *S*3 that were annealed at 493 K and 673 K, respectively, leading to different Mn_5Si_3 concentrations [see Fig. 4(b)]). The red (blue) color indicates 100% of the Mn_5Si_3 (MnSi). The data points are shown by the green dots. (b) Effect of T_A on the Mn_5Si_3 concentration in thin films grown with $R_{Mn/Si} = 1.6$ and $T_G = 443$ K. The specific samples detailed in Secs. III A and III B are shown on these graphs.

in Fig. 4(b). The MnSi formation could be hampered by limiting T_A to 493 K. In the following, the structural properties of the Mn-Si thin films were systematically studied to give a comprehensive picture of the phase formation mechanisms.

B. From Mn_5Si_3 to MnSi

We first consider the case of the pure Mn_5Si_3 thin film obtained with $R_{Mn/Si} = 1.6$, $T_G = 443$ K and a subsequent annealing at 493 K. This sample is so-called *S*1 [see Fig. 4(b)]. Figures 5(a) to 5(c) show the RHEED images taken along the direction corresponding to the Si(111)-[1$\bar{1}$0] azimuth at various stages of the Mn_5Si_3 growth. The Si(111)-(7 × 7) reconstruction disappears at the first stage of the growth. After the codeposition of 1.5 nm of Mn-Si, the intensity of the Si reflections completely disappeared to give rise to a diffuse pattern that is characteristic of an amorphous layer [Fig. 5(a)]. This blurry pattern persisted during the deposition of the following 10 nm before a faint RHEED pattern appears, as shown in Fig. 5(b). An annealing up to 493 K significantly improved the surface crystallinity, as shown in Fig. 5(c). The streak spacing is consistent with the formation of Mn_5Si_3. The modulated streak intensity of the RHEED pattern was assigned to a multistepped surface [45]. This is consistent with the topography characterization by AFM [Fig. 5(f)] that revealed the presence of small terraces leading to an average roughness of 0.9 nm. A similar morphological behavior was observed in the isostructural Mn_5Ge_3 grown on Ge(111) by low-temperature codeposition [46] and was mainly attributed the surface preparation and buffer deposition.

High-resolution TEM (HRTEM) was carried to study the structural properties of the thin film and the interfacial region. Figure 5(d) shows a cross-sectional HRTEM image of the Mn_5Si_3/Si heterostructure. The investigated film exhibited an atomically sharp interface. Two crystalline columns with a conical shape were observed. The spacing between vertical planes matched the Mn_5Si_3 crystal. In these regions, the zone axis was identified as [2$\bar{1}\bar{1}$0] with the Mn_5Si_3[0001] growth direction parallel to Si[111]. This is fully consistent with the established epitaxial relationships using RHEED and XRD techniques. Surprisingly, no atomic resolution in the Mn_5Si_3 phase could be observed at the vicinity of the interface with the substrate. Crystalline Mn_5Si_3 seems to grow from the volume of the codeposited film. At the top of the layer, the columns reached a width of about 15 nm. Between these two columns, a grain showed weak contrast, presenting a slightly different zone axis. The XRD pattern of the corresponding thin film [Fig. 2(a)] displayed circle-arc Bragg reflexions of about ±5°, which is indicative of the average grain misorientation around the growth direction. The crystal structure parameters were determined by analyzing the measurements coming from the various techniques. The in-plane and out-of-plane lattice constants were found to be: $a = (6.94 \pm 0.02)$ Å and $c = (4.78 \pm 0.02)$ Å, respectively. Despite the +3.7% lattice mismatch between Mn_5Si_3 and Si(111), the structure appeared almost relaxed at room temperature.

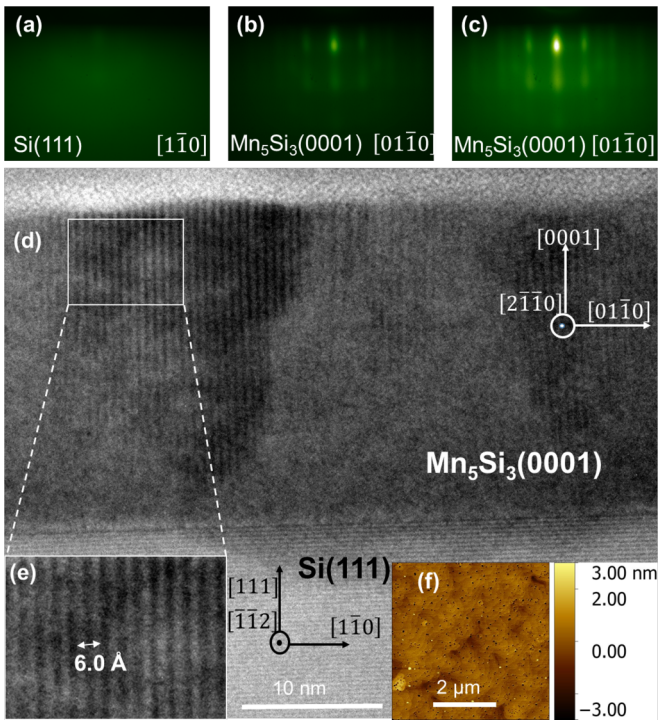

FIG. 5. Structural properties of thin films containing only the Mn_5Si_3 phase (so-called *S*1 sample). $T_G = 443$ K and $R_{Mn/Si} = 1.6$. [(a)–(c)] RHEED patterns of the surface taken along the direction corresponding to the Si(111)-[1$\bar{1}$0] azimuth at the intermediate amorphous stage during the growth process, at the end of codeposition and after the mild annealing up to 493 K, respectively. (d) High-resolution transmission electron microscopy image showing a ∼20-nm-thick $Mn_5Si_3$with (e) a zoom on the Mn_5Si_3 phase. (f) AFM image corresponding to an average roughness of 0.9 nm.

Increasing the annealing temperature significantly improved the crystalline quality as indicated by the brighter and thinner streaks shown in Figs. 6(c) and 6(d) for a sample annealed up to 573 K (*S*2 sample). XRD confirmed the enhancement of the structural properties with well-defined Mn_5Si_3 diffraction spots and a subsequent reduced FWHM. However, the thin film was no longer monophase and contained, in addition to Mn_5Si_3, a small amount of the MnSi compound. Cross-sectional TEM [Figs. 6(a) and 6(b)] indicated that the phase is located between the Si(111) and Mn_5Si_3 with a sharp interface with the Si substrate. A closer study of the interfacial region showed a periodic intensity contrast corresponding to an array of dislocations [46,47]. It is particularly visible along the Si(111)-[11$\bar{2}$] direction [see Fig. 7(a)] with an occurrence of 17 nm, corresponding to 26 unit cells. This arrangement allows to partially accommodate the −3% in-plane lattice mismatch between Si and MnSi. A slight tensile strain of 0.86% remains, in good agreement with previous works [41,47]. The elongated shape of the MnSi(111) reflection in XRD measurements indicates a thickness-dependent out-of-plane lattice parameter, that has been calculated to be in average −0.35%. This crossover region in which the residual strain is relaxed has been already observed in the MnSi/Si(111) heterostructure grown using SPE [41,47]. Surprisingly, despite the +6.7% lattice mismatch between MnSi and Mn_5Si_3, MnSi acts as a seed layer for the oriented single crystalline growth of Mn_5Si_3. The crystal quality is good despite a irregular interface. From RHEED, XRD and TEM cross-analysis, the *a* and *c* lattice parameters have been estimated to (6.93 ± 0.03) Å and (4.80 ± 0.02) Å at room temperature. This almost relaxed structure is assigned to strain relief in highly mismatched systems.

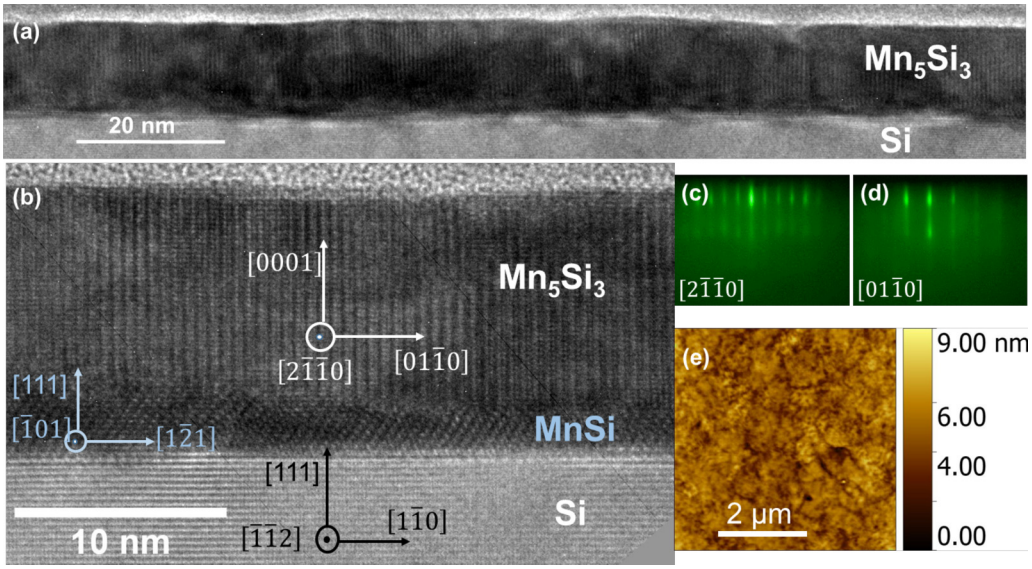

FIG. 6. Structural properties of thin films deposited with a Mn/Si flux ratio of 1.6 at a temperature $T_G = 443$ K and annealed up to 573 K (*S*2 sample). (a) Enlarged view of the HRTEM cross-section of a 13-nm-thick Mn_5Si_3 thin film (b) and zoom at the vicinity of the interface. An interfacial MnSi layer with a thickness of 1.5–2 nm is sandwiched between the Si(111) substrate and the Mn_5Si_3 thin film. [(c), (d)] RHEED patterns of the final surface taken along the Mn_5Si_3 (0001)-[2$\bar{1}\bar{1}$0] and [01$\bar{1}$0] azimuths, respectively. (e) AFM image of the Mn_5Si_3 surface sample with a corresponding average roughness of 0.7 nm.

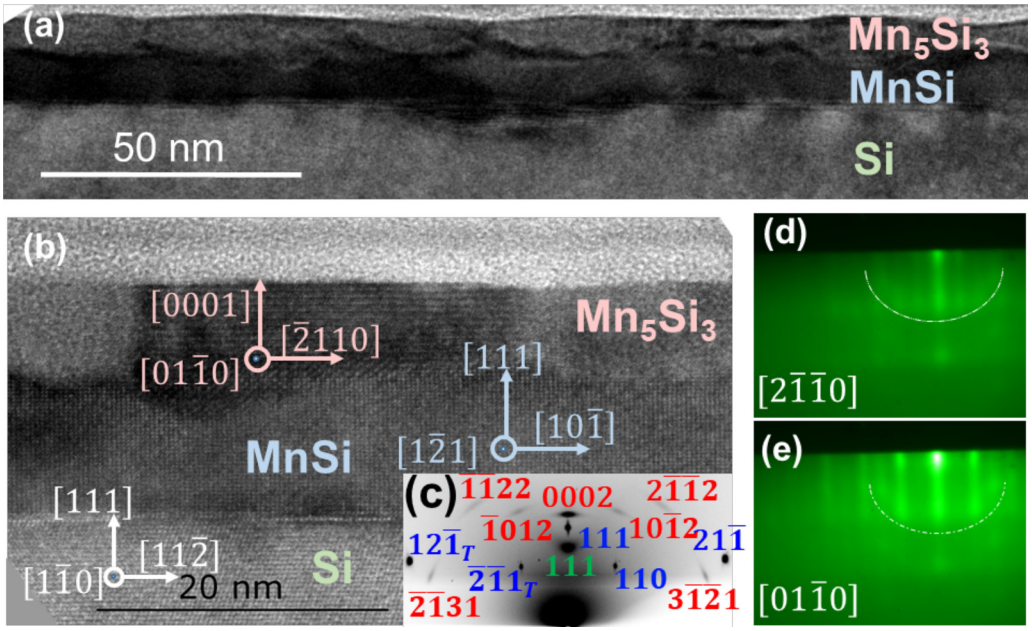

FIG. 7. (a) Enlarged view and (b) zoom around the interface of the HRTEM cross-section of a 17-nm-thick film (*S*3 sample) grown with $T_G = 443$ K and $R_{Mn/Si} = 1.6$ and subsequently annealed up to 673 K. (c) Corresponding 2D-XRD pattern revealing a crystalline MnSi film and a textured Mn_5Si_3 overlayer. [(d), (e)] RHEED patterns of the final surface taken along the Mn_5Si_3 (0001)-[2$\bar{1}\bar{1}$0] and [01$\bar{1}$0] azimuths, respectively. Brighter spots are distributed on a half elliptical ring indicated by a thin dotted line, which indicated the presence of slightly misoriented grains.

Annealing at a higher temperature leads to an increase of the MnSi content as shown in the HRTEM images of Figs. 7(a) and 7(b) for a sample annealed up to 673 K (*S*3 sample). Concomitantly, the Mn_5Si_3 crystallinity deteriorates as pointed out by the circle-arcs-shaped Bragg peaks in the 2D-XRD map [Fig. 7(c)]. Corresponding RHEED images [Figs. 7(d) and 7(e)] show Mn_5Si_3 surface diffraction patterns intermixed with a faint elliptical ring that passes through brighter spots. This indicates a transition towards a polycrystalline structure. HRTEM images confirm both the preponderance of the MnSi phase and the Mn_5Si_3 crystallinity deterioration. The MnSi film is a highly ordered epitaxial structure on the Si(111) substrate. The interface between substrate and film is still sharp, albeit not as atomically flat as previously (Figs. 5 and 6). This suggests a local Mn and Si interdiffusion at the interface vicinity. In contrast, Mn_5Si_3 grains with a width of about 20 nm nucleated from the wavy MnSi/Mn_5Si_3 interface. The Mn_5Si_3 structure is textured with the *c*-axis still lying preferentially along the Si[111]. A longer annealing induced the formation of a full MnSi thin film.

Any deviation from the ideal stoichiometry for Mn_5Si_3 favors the preferential formation of MnSi. In Mn rich films, no RHEED pattern appeared during the growth, which is characteristic of an amorphous layer. Obtaining a crystalline phase required an annealing step at temperature higher than 673K. The heating process caused the interdiffusion and a Si enrichment of the thin films, which favored the formation of MnSi. In Mn deficient samples but still above the "1" ratio, MnSi is formed either during the growth for ratio close to one or after a mild annealing (generally below 573 K).

The effect of the substrate temperature during the growth (T_G) was also investigated for a Mn/Si ratio of 1.6. A temperature higher than 473 K leads to the formation of MnSi due to a non neglectible Si diffusion and nucleation at the interface. For T_G lower than 423 K, a longer annealing was required to get any RHEED pattern and therefore the phase formation. A temperature of 443 K was found to be the best compromise to allow Mn_5Si_3 nucleation from an interface while limiting Mn and Si interdiffusion.

C. Competing phase formation and Mn_5Si_3 stabilization

As described above, the epitaxial growth of Mn_5Si_3 thin films onto Si substrates requires careful control of the growth conditions. The reaction of the deposited Mn-Si layer deposited on silicon and the subsequently forming phase depend on the Mn and Si deposition rates (characterized by $R_{Mn/Si}$), and the substrate temperature during deposition (T_G) and annealing (T_A). These parameters determine the local intermixing at the interface and drive the growth of a compound that is in equilibrium with the silicon substrate. The reaction path for a process to take place is driven by the change in the Gibbs free energy: $\Delta G = \Delta H - T\Delta S$ where ΔH is the change in heat formation during the reaction occurring at a temperature T and ΔS is the change in entropy. For solid state reactions, $\Delta G \sim \Delta H$. In this context, the Walser-Béné (WB) model was widely used to predict the first nucleating phase in metal-silicon (M-Si) systems, using thermodynamic data [48]. The effective heat of formation (EHF) model extends and supplements the WB rule improved by Ronay [49]. In this thermodynamic-kinetic framework, the local concentrations of atoms available to participate in the reaction are considered. The first phase to nucleate in SPE is therefore the congruent phase next to the eutectic closest to the center of the phase diagram of the M-Si couple (in atomic percent) and exhibiting the lowest effective heat of formation ($\Delta H'$) [49,50]. Regard-

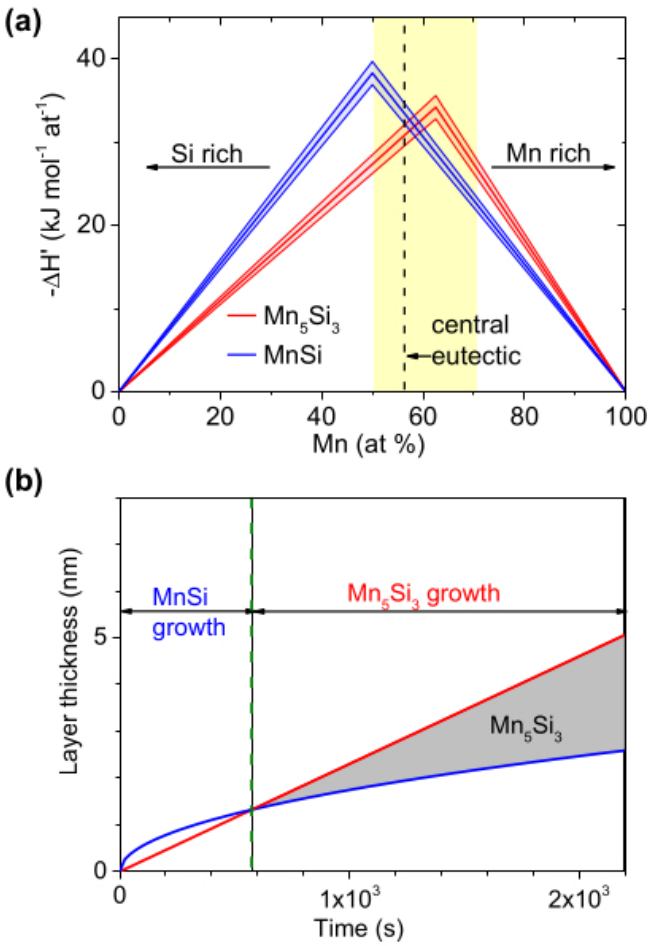

FIG. 8. (a) Effective heat of formation diagram of MnSi and Mn_5Si_3 constructed from the enthalpies extracted from reference [52]. The thin blue and red lines are error margins. The dashed line indicates the position of the central eutectic. The colored band displays the investigated stoichiometries in this work. (b) Schematic illustration of the MnSi and Mn_5Si_3 formation at a given annealing temperature. The thin blue line represent the calculated MnSi layer thickness in the diffusion-controlled reaction using diffusion coefficients from Ref. [56]. The thick red line shows the linear dependence of the Mn_5Si_3 growth that is controlled by the rate of reaction [57]. Mn_5Si_3 nucleates on the MnSi surface when the MnSi layer is thick enough to hamper the crossdiffusion of Mn and Si.

ing the Mn-Si binary diagram, the temperature of the lowest eutectic is 1373 K at a Mn concentration of 79.8% [51]. Two other eutectics exist: one at 1422 K and 33.6 Mn% and the second one, being the one closest to the center of the phase diagram, at 1510 K and 56.2 Mn at%. The MnSi and Mn_5Si_3 phases are both congruent phases at melting temperatures of 1543 K and 1556 K, respectively. Using the enthalpies of formation from Ref. [52], we drew the effective heat of formation diagram for MnSi and Mn_5Si_3 compound [Fig. 8(a)]. At the central eutectic, their respective effective heat of formation are $-(33.7 \pm 1.4)$ kJ (mol at)$^{-1}$ and $-(30.6 \pm 1.4)$ kJ (mol at)$^{-1}$. This implies that, in the case of SPE, MnSi is slightly more favorable than Mn_5Si_3, which is in agreement with studies reported in literature [41,42,47,53–55]. However, for a Mn and Si codeposition growth process, the triangle diagram of Fig. 8(a) shows that it is possible to shift artificially the phase formation toward Mn_5Si_3 favorable condition by tuning the relative value of the deposition flux. This was done in this work by setting $R_{Mn/Si}$ to 1.6.

These thermodynamically based considerations are not sufficient to describe the growth process and important features such as interface free energy and the generation of nonequilibrium structures, including amorphous phase, are not taken into account in this simple picture. Assuming that the nucleation of compounds at the metal-silicon interface is a kinetically governed process, it was shown that the interfacial M-Si region which presents a free energy higher than the mixed state undergoes a structural transition that maximizes its free-energy lowering rate [58,59]. A phase with its two associated interfaces, so-called interphase, is favorable in the reaction if it has a higher growing rate and leads to a greater free-energy decrease during the initial stage of the reaction [59]. This approach emphasizes the kinetics limited regime in the phase growth process.

From the presented data in Sec. III B and the foregoing discussion, a detailed model of the growth of Mn_5Si_3 thin films on Si(111) is now proposed. In the codeposition process, we investigate the reaction at the interface between Si(111) and an intermixing Mn-Si layer with a fixed composition close to the Mn_5Si_3 phase. We first consider the case of a limited-diffusion reaction, so-called stage I, in which chemical species diffuse only in their atomic neighborhood. This condition is fullfilled in this work for a growth temperature of ∼443 K. The initial kinetically preferred local chemical structure corresponds to a glassy central phase as shown in Fig. 5. The amorphous state can have a higher growth rate if the competing crystalline phase cannot nucleate [60]. The interface energy between Mn_5Si_3 and Si compounds is presumably high. Calculations should be performed to determine this value. However, a direct Mn_5Si_3/Si(111) interface was observed only during the solid state reaction of a Mn thin film deposited on Si(111)-$(\sqrt{3} \times \sqrt{3})$R30°:Bi surface [61] where the reconstruction heavily modifies the interface energy and the species diffusion through it. The direct reaction of a Mn layer on Si(111) inevitably leads in the first place to MnSi formation [41,42,47,53,55]. In the present growth conditions, the low temperature process limits diffusion at the initial interface, hindering the nucleation process. The metastable glassy phase with a local bonding pattern and concentration close to those of Mn_5Si_3 is therefore expected to minimize interface energy. This phase continues to increase in layer thickness until a kinetic instability occurs suddenly and a diffusionless transformation takes place [62]. The nucleation of the crystalline structure reduces the energy of the system faster than the continued growth of the original phase. This instability occurs at a thickness of about 2–5 nm from the interface, which is in good agreement with a diffusion-controlled growth model [58,59].

A higher substrate temperature during either the deposition or the annealing stage favors diffusion and local Si enrichment at the vicinity of the interface region, which drives the thermodynamic equilibrium toward MnSi. As already mentioned, the selective growth of a particular phase by a solid state reaction is mainly triggered by the interface composition that is governed by the diffusion flux to the interface. In our work,

we found the formation of epitaxial MnSi on Si(111) for a growth or annealing temperature above 493 K. This is in line with the study of the reaction of a Mn thin films deposited on Si(111) showing the formation of MnSi from the initial stage of the growth [53,55]. The stability of MnSi thin films on Si(111) was also investigated theoretically. The B20-like film with a formation energy of 76 meV/Å^{-2} [63], is found to be the most stable structure in full agreement with the experimental observation of $(\sqrt{3} \times \sqrt{3})$R30°-reconstructed films [53] indicative of MnSi in the B20 structure. The B20 MnSi(111) structure consists of a sequence of a Si-dense, Mn-sparse, Si-sparse, and Mn-dense layers. The bonding of the MnSi film on Si(111) with the substrate is presumably made by a Si-dense layer to minimize the interface energy under the locally Si-rich conditions present at the interface to the substrate [42,63]. This is consistent with the formation of a eutectic alloy between MnSi and Si that is a good indication of a low interfacial free energy, and thus it is a strong indication of an easy nucleation [49]. TEM images (Figs. 6 and 7) showed that thin films of MnSi were grown epitaxially. The −3% lattice mismatch between Si and MnSi is partially accommodated by the formation of a dislocation network at the interface, still resulting in some tensile residual strain in the MnSi film close to the interface. Interestingly, the MnSi intermediate layer changed the boundary condition for the metastable glassy Mn_5Si_3 and made favorable the nucleation of crystalline Mn_5Si_3 as illustrated in the stage II of Fig. 9. The driving force is a rapid decrease of the free energy induced by the formation of crystalline phases. This finding suggests a low-energy interface suitable for the nucleation of Mn_5Si_3. Concerning the crystallographic relationships of the resultant deposit, the MnSi film satisfied the conventional reported orientation [41]. Remarkably, the Mn_5Si_3 epilayer adopted the same orientation as the isostructural Mn_5Ge_3 grown on Ge(111) in spite of the interfacial undesired compound. The *c*-axis was found perpendicular to the surface with a rotation of 30° of the Mn_5Si_3 unit cell with respect to the Si(111) one. The lattice mismatch between Mn_5Si_3 (0001) and Si(111) being +3.7%, the resulting mismatch between MnSi and Mn_5Si_3 is large—up to 6.7% if the two phases are fully relaxed—but still permits epitaxial growth.

At a constant substrate temperature, the reaction layer thickness depends on the deposition rates and on the growth- or annealing-time (t). According to previous works [56,64], the MnSi reaction is diffusion-controlled with Si as the major diffuser in MnSi [28]: the thickening of the MnSi layer is therefore proportional to the square root of the product $(D \times t)$ where D is the temperature-activated cross-diffusion coefficient [blue line in Fig. 8(b)]. Using the activation energy and the diffusion coefficient of Si in MnSi from Ref. [56], it can be shown that no significant diffusion occurs before 523 K, which fits well with our experimental finding. The phase formation mainly occurs during the annealing stage [stage III of Fig. 9]. This diffusion-based model predicts a MnSi thickness of 1.5 nm for an annealing of 600 s at T_A = 573 K ($D \approx 0.8 \times 10^{-22}$ m^2/s), which is in good agreement with our experimental data. However, a linear growth regime is expected for Mn_5Si_3 as expected in systems governed by phase nucleation and growth without long-range atomic transport [57]. This is schematically represented in Fig. 8(b) by the thick red line. The lack of available data on the kinetics of the Mn_5Si_3 phase nucleation makes it impossible to quantitatively predict the crossover between the MnSi and Mn_5Si_3 growth regime. However, this simple picture explains why the critical thickness is therefore extremely dependent on the growth conditions. Increasing the substrate temperature (T_G or T_A) favored cross-diffusion and resulted in a thicker MnSi film. This is consistent with Fig. 4(a) showing the predominant growth of MnSi at high T_G.

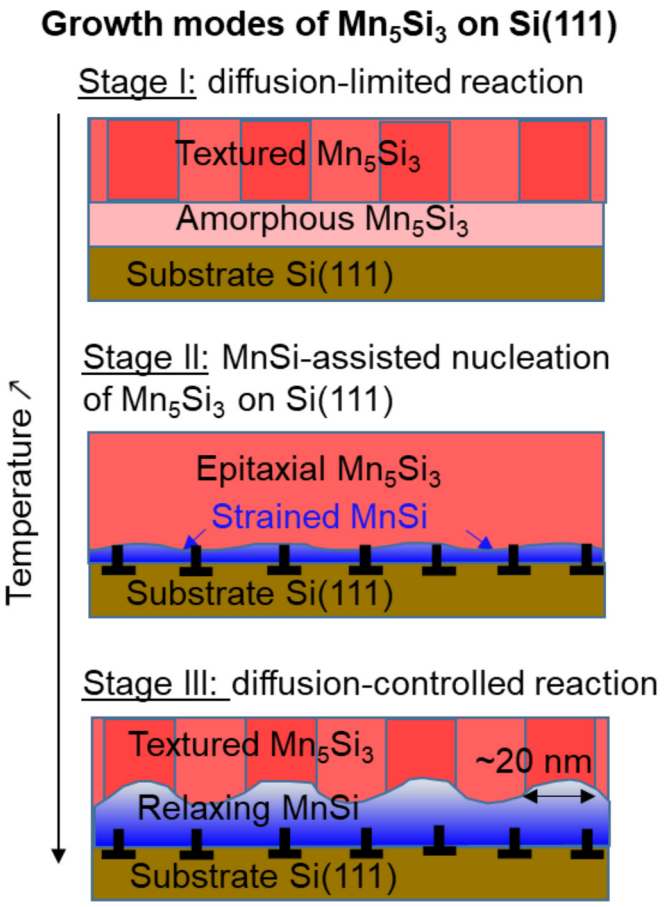

FIG. 9. Schematic representation of the competitive growth in Mn_5Si_3 /Si(111) heterostructure either between amorphous and crystalline Mn_5Si_3 (stage I) or between MnSi and Mn_5Si_3 crystalline films (stage II). A thicker layer of MnSi induces a texturing of the Mn_5Si_3 overlayer (stage III). Partial film relaxation is achieved either by interfacial dislocations represented by the bold inverted-T symbols or by interface/surface roughening.

The MnSi thickening was accompanied by an augmentation of roughness of the top interface with Mn_5Si_3. This was assigned to the relaxation of the residual strain of the MnSi lattice. Previous works reported on similar surface modulation with a periodicity of about 20 nm [53,54]. In our case, this interface corrugation led to the formation of a textured Mn_5Si_3 film in spite of the good quality of the MnSi underlayer. The grains with a size determined by the surface undulation were slightly misoriented, allowing to accommodate the highly mismatch between the two materials, as shown in Fig. 7 in a heterostructure annealed up to 673 K.

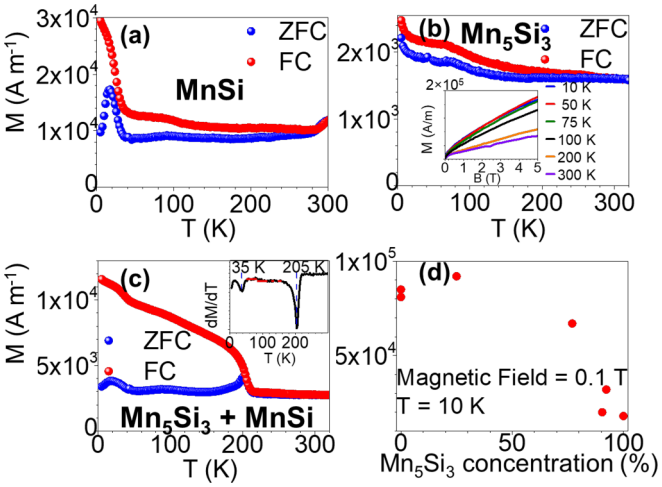

FIG. 10. Temperature dependence of magnetization measured at 100 Oe, in ZFC and FC regimes, with magnetic field applied parallel to the thin film plane for (a) a MnSi(111) film grown on Si(111); (b) a Mn_5Si_3 film grown on Si(111), and (c) a mixed-phase layer containing 23% MnSi and 77% Mn_5Si_3. The corresponding derivative curve, shown in the inset of panel (c), clearly indicates the magnetic transitions of both the phases. The inset in panel (b) shows the corresponding M-H curves collected with an in-plane applied field at various temperatures. (d) Magnetization values at 10 K and with an in-plane magnetic field of 0.1 T for samples containing various concentrations of Mn_5Si_3.

Conversely, for a T_G lower than 423 K, the diffusion was too low to obtain a local bonding pattern in the growing glass phase notwithstanding the respect of the Mn_5Si_3 stoichiometry. A diffusionless transformation cannot take place. Transformation into a crystalline structure required an annealing step that, in turn, activated the diffusion and the subsequent MnSi formation.

On the issue of nonstoichiometric deposit, species intermixing and phase nucleation were required to form a crystalline layer. The first process was governed by diffusion that is mostly temperature driven. The Si reservoir at the vicinity of the interface, its low formation enthalpy and interfacial energy with Si(111) promoted the formation of MnSi.

IV. TRACKING MN-SI STRUCTURAL PROPERTIES WITH MAGNETIC AND TRANSPORT MEASUREMENTS

A. Magnetic properties

Figure 10 shows the zero-field-cooled (ZFC) and field-cooled (FC) temperature dependence of the volume magnetization for different manganese silicide thin films: a 13-nm-thick MnSi film, a 27-nm-thick thick Mn_5Si_3 film (*S*1 sample), and a 20-nm-thick thick MnSi + Mn_5Si_3 mixed-phase film. The measurements were carried out with an in-plane magnetic field of 100 Oe. The transition temperatures were determined as the inflexion point of the FC curve. Both MnSi and Mn_5Si_3 exhibit very distinct magnetic signatures with characteristic transition temperatures and magnetization values. As shown in Fig. 10(a), the magnetization (M) of the MnSi film drops significantly for temperatures above 20 K, indicating a ferromagnetic transition temperature (T_C) close to bulk MnSi ($T_C \sim 30$ K) [65]. This is also in good agreement with previous reports for MnSi single- and polycrystalline thin films [47,66]. In addition, a weak ferromagnetic signal persisted up to ∼290 K. The presence of a second ferromagnetic phase with a T_C value close to room temperature has been already reported in MnSi(111)/Si(111) system [67,68] and has been attributed to the interface.

In contrast, the zero-field-cooled and field-cooled (ZFC-FC) curves for Mn_5Si_3 show no abrupt transitions [Fig. 10(b)]. They exhibit splitting below ∼240 K and an increase in M down to 70 K. Further decrease in sample temperature results in little change in the M value until 20 K, the temperature below which M increases sharply in both FC and ZFC curves. In the parent bulk material, a transition to a collinear Néel antiferromagnetic phase is reported at 100 K [8,69]. In our case, the corresponding PM-to-AF2 transition seems to appear at higher temperature (above 200 K). A second feature in the M-T curve is also expected at low temperature (∼70 K) at the AF2/AF1 crossover. Again, distinct from bulk material where a sharp transition is measured at 70 K [70,71], a change of slope in the M-T curve is observed here. It is worth noting that similar M-T trends have been observed in the polycrystalline thin films for fields below 1 T [16].

The antiferromagnetic characteristic is supported by the dependence of magnetization on the applied magnetic field shown in the inset of Fig. 10(b). All the M-H curves are found to be antisymmetric around the origin and only the positive branches are shown here. M is vanishing at zero-field as expected in an AF compound. Its magnitude rises with increasing field with a small negative curvature and does not saturate in our maximum field of 5 T. Interestingly, the magnetization at 50 K is higher than the one at 10 K for $H \geqslant 2$ T. This feature is attributed to the temperature-dependent transition AF1/AF2 that appeared at lower field for higher temperature [72], which highlights the Mn_5Si_3 complex spin structure that is both field- and temperature-dependent.

In samples with a mixture of MnSi and Mn_5Si_3, the M-T curve [Fig. 10(c)] exhibits clear magnetic transitions as defined by the two minima of the dM/dT curve shown in the inset for a sample with a Mn_5Si_3 concentration of 77%. Although the exact transition temperatures are sample-dependent, the first one is around 35 K, whereas the second one occurs in the 200–240 K range. These characteristic temperatures represent a direct signature of the MnSi and Mn_5Si_3 phases, respectively. The PM-AF2 transition in the two-phase compound is much sharper than in the pure Mn_5Si_3 thin film and its magnetization is slightly enhanced. This probably results from the better crystallinity of Mn_5Si_3 in the presence of the MnSi seed layer. However, the transition around 70 K is barely perceptible, with only a sluggish slope change around 70 K as indicated by the two plateaus on the dM/dT curve. This magnetic transition is nonetheless present in our films that exhibit a THE below 70 K as shown in Ref. [17]. The magnetization measurements reflect the sample composition. For instance, the magnetization value at 10 K can be used as an indicator of the Mn_5Si_3 content as shown in Fig. 10(d). These exploratory results on the Mn_5Si_3 magnetic properties are indicative of a complex material with a field- and temperature-dependent spin structure that, however, is distinct from the parent bulk compound, especially concerning the

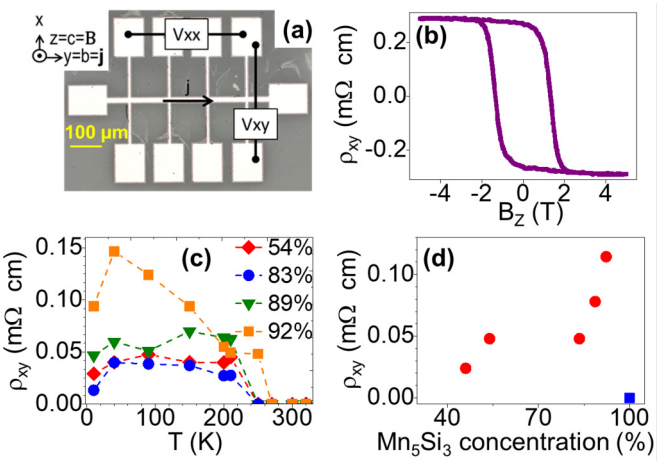

FIG. 11. (a) Optical micrograph of the lithographically patterned Hall bar showing the orientation of the applied magnetic field B_z and the measured longitudinal and transverse signal. (b) Anomalous Hall resistivity in the antiferromagnetic phase measured at 130 K. The ordinary Hall effect, which is linear in the applied magnetic field B_z, was subtracted. (c) Temperature dependence of the Hall resistivity for various samples. (d) Measured Hall resistivity as a function Mn_5Si_3 concentration for crystalline (red point) and polycrystalline (blue square) samples.

transition temperatures. The full magnetic characterization of Mn_5Si_3 thin films is beyond the scope of this study and will be reported in a separated paper.

B. Transport properties

A microscope image of a typical Hall bar and the experimental geometry is shown in Fig. 11(a). Figure 11(b) exemplarily shows the measured anomalous Hall signal at 130 K in a sample with high ratio of Mn_5Si_3. A clear hysteresis and a strong spontaneous signal at $B = 0$ T is in striking contrast to the magnetometry data, the latter showing vanishing remanent magnetization and no coercivity. Unlike in common ferromagnets, the robust spontaneous anomalous Hall signal in Mn_5Si_3 arises from crystal and spin symmetry which macroscopically breaks the time reversal symmetry despite the absence of net magnetization, as we reported in Ref. [17]. Because not only the magnetic order of the material, but also its crystal symmetry are the prerequisites for the time reversal symmetry breaking in the band structure, the quality of the Mn_5Si_3 crystal is of key importance for the presence of the anomalous Hall effect. The magnetotransport measurements, therefore, can serve as a complementary tool to determine the film quality in terms of crystallinity and the ratio between Mn_5Si_3 and MnSi. Several samples were prepared by MnSi assisted nucleation of the Mn_5Si_3 on Si(111) and the anomalous Hall resistivity was measured at various temperatures as shown in Fig. 11(c). All studied samples share a similar general trend – a robust anomalous Hall resistivity below 240 K and the absence of such a Hall signal above this temperature. There is, however, a large scatter of the sample dependent anomalous Hall resistivity as evident from Fig. 11(c). To understand this variation, the anomalous Hall resistivity measured in various samples at 150 K is plotted against the Mn_5Si_3 /MnSi ratio measured by XRD in Fig. 11(d). The data suggest a clear correlation: ration of Mn_5Si_3 around 95% (i.e., higher film quality) corresponds to higher amplitude of the anomalous Hall effect. It is also worth noting that the magnetotransport response of a polycrystalline Mn_5Si_3 was measured. Interestingly, this sample did not show any clear anomalous Hall effect [blue square in Fig. 11(d)].

V. CONCLUSIONS

In this work, the epitaxial growth of monocrystalline Mn_5Si_3 thin films was achieved using a codeposition process in a MBE chamber with carefully controlled parameters. The Mn_5Si_3/Si(111) heteroepitaxial growth followed the $Mn_5Si_3(0001)[01\bar{1}0]//Si(111)[1\bar{1}0]$ orientation through a complex interface composed either of an amorphous phase or a MnSi layer. The interface energy is presumably too high to ensure the direct nucleation of Mn_5Si_3 on Si(111). DFT calculations should be performed to verify this assumption. Interface engineering using a thin seed layer could lower this energy and act as a diffusion barrier [34,61]. As a further general comment, the growth strategy used in the present study could potentially open up more efficient routes for depositing epitaxial films for nanoscaled electronic and magnetic devices.

The growth of high-crystalline quality Mn_5Si_3 thin films has been here achieved by means of the formation of a thin MnSi layer at the Si/Mn_5Si_3 interface. The action of MnSi is therefore dual: it is beneficial in terms of assisting the Mn_5Si_3 nucleation on Si(111) but detrimental to the Mn_5Si_3 crystal quality as soon as its thickness exceeds few nanometers, in other words when the built-in strain starts to be relaxed.

A spontaneous anomalous Hall effect is observed in crystalline Mn_5Si_3 thin films grown on Si(111), which stems from a peculiar crystal and spin arrangement, stabilized by epitaxy. Magnetic characterizations and transport measurements can act as sensitive probes of the sample composition and its correlated crystallinity. Mn_5Si_3/Si(111) thin films therefore open a promising new avenue in the search of emerging altermagnetic spintronics with light elements.

ACKNOWLEDGMENTS

This work was supported by the French national research agency (ANR) and the Deutsche Forschungsgemeinschaft (DFG) (Project MATHEEIAS- Grant No. ANR-20-CE92-0049-01 / DFG-445976410). H.R. and E.S. acknowledge GACR Grant No. 22-17899K. D.K. acknowledges the Lumina Quaeruntur fellowship of the Czech Academy of Science (Grant No. LQ100102201). L.S. and J.S. acknowledge Elasto-Q-Mat (DFG SFB TRR 288).

[1] L. Liu, H. Oda, T. Onda, N. Yodoshi, T. Wada, and Z.-C. Chen, Microstructure and thermoelectric properties of higher manganese silicides fabricated via gas atomization and spark plasma sintering, Mater. Chem. Phys. **249**, 122990 (2020).

[2] S. Mühlbauer, B. Binz, F. Jonietz, C. Pfleiderer, A. Rosch, A. Neubauer, R. Georgii, and P. Böni, Skyrmion lattice in a chiral magnet, Science **323**, 915 (2009).

[3] T. Yokouchi, N. Kanazawa, A. Tsukazaki, Y. Kozuka, A. Kikkawa, Y. Taguchi, M. Kawasaki, M. Ichikawa, F. Kagawa, and Y. Tokura, Formation of in-plane skyrmions in epitaxial MnSi thin films as revealed by planar Hall effect, J. Phys. Soc. Jpn. **84**, 104708 (2015).

[4] C. Pfleiderer, J. Boeuf, and H. v. Löhneysen, Stability of antiferromagnetism at high magnetic fields in Mn_3Si, Phys. Rev. B **65**, 172404 (2002).

[5] F. Steckel, S. Rodan, R. Hermann, C. G. Blum, S. Wurmehl, B. Büchner, and C. Hess, Spin density wave order and fluctuations in Mn_3Si: A transport study, Phys. Rev. B **90**, 134411 (2014).

[6] P. Brown, J. Forsyth, V. Nunez, and F. Tasset, The low-temperature antiferromagnetic structure of Mn_5Si_3 revised in the light of neutron polarimetry, J. Phys.: Condens. Matter **4**, 10025 (1992).

[7] P. Brown and J. Forsyth, Antiferromagnetism in Mn_5Si_3: The magnetic structure of the AF2 phase at 70 k, J. Phys.: Condens. Matter **7**, 7619 (1995).

[8] M. Gottschilch, O. Gourdon, J. Persson, C. de la Cruz, V. Petricek, and T. Brueckel, Study of the antiferromagnetism of Mn_5Si_3: An inverse magnetocaloric effect material, J. Mater. Chem. **22**, 15275 (2012).

[9] N. Biniskos, F. J. dos Santos, K. Schmalzl, S. Raymond, M. dos Santos Dias, J. Persson, N. Marzari, S. Blügel, S. Lounis, and T. Brückel, Complex magnetic structure and spin waves of the noncollinear antiferromagnet Mn_5Si_3, Phys. Rev. B **105**, 104404 (2022).

[10] C. Sürgers, T. Wolf, P. Adelmann, W. Kittler, G. Fischer, and H. V. Löhneysen, Switching of a large anomalous Hall effect between metamagnetic phases of a noncollinear antiferromagnet, Sci. Rep. **7**, 1 (2017).

[11] M. Gajdzik, C. Sürgers, M. Kelemen, and H. V. Löhneysen, Ferromagnetism in carbon-doped Mn_5Si_3 films, J. Appl. Phys. **87**, 6013 (2000).

[12] C. Sürgers, M. Gajdzik, G. Fischer, H. V. Löhneysen, E. Welter, and K. Attenkofer, Preparation and structural characterization of ferromagnetic $Mn_5Si_3C_x$ films, Phys. Rev. B **68**, 174423 (2003).

[13] M. Gajdzik, C. Sürgers, M. Kelemen, and H. Löhneysen, Strongly enhanced Curie temperature in carbon-doped Mn_5Ge_3 films, J. Magn. Magn. Mater. **221**, 248 (2000).

[14] A. Spiesser, I. Slipukhina, M.-T. Dau, E. Arras, V. Le Thanh, L. Michez, P. Pochet, H. Saito, S. Yuasa, M. Jamet, and J. Derrien, Control of magnetic properties of epitaxial $Mn_5Ge_3C_x$ films induced by carbon doping, Phys. Rev. B **84**, 165203 (2011).

[15] S. Deng, R. Heid, K.-P. Bohnen, C. Wang, and C. Sürgers, Minority-spin conduction in ferromagnetic $Mn_5Ge_3C_x$ and $Mn_5Si_3C_x$ films derived from anisotropic magnetoresistance and density functional theory, Phys. Rev. B **103**, 134439 (2021).

[16] C. Sürgers, G. Fischer, P. Winkel, and H. V. Löhneysen, Large topological Hall effect in the noncollinear phase of an antiferromagnet, Nat. Commun. **5**, 3400 (2014).

[17] H. Reichlová, R. L. Seeger, R. González-Hernández, I. Kounta, R. Schlitz, D. Kriegner, P. Ritzinger, M. Lammel, M. Leiviskä, V. Petříček *et al.*, Macroscopic time reversal symmetry breaking by staggered spin-momentum interaction, arXiv:2012.15651v2.

[18] L. Šmejkal, R. González-Hernández, T. Jungwirth, and J. Sinova, Crystal time-reversal symmetry breaking and spontaneous Hall effect in collinear antiferromagnets, Sci. Adv. **6**, eaaz8809 (2020).

[19] L. Šmejkal, J. Sinova, and T. Jungwirth, Emerging research landscape of altermagnetism, Phys. Rev. X **12**, 040501 (2022).

[20] L. Šmejkal, J. Sinova, and T. Jungwirth, Beyond Conventional Ferromagnetism and Antiferromagnetism: A Phase with Nonrelativistic Spin and Crystal Rotation Symmetry, Phys. Rev. X **12**, 031042 (2022).

[21] L. Šmejkal, A. B. Hellenes, R. González-Hernández, J. Sinova, and T. Jungwirth, Giant and tunneling magnetoresistance effects from anisotropic and valley-dependent spin-momentum interactions in antiferromagnets, Phys. Rev. X **12**, 011028 (2022).

[22] R. González-Hernández, L. Šmejkal, K. Výborný, Y. Yahagi, J. Sinova, T. Jungwirth, and J. Železný, Efficient Electrical Spin Splitter Based on Nonrelativistic Collinear Antiferromagnetism, Phys. Rev. Lett. **126**, 127701 (2021).

[23] D.-F. Shao, S.-H. Zhang, M. Li, and E. Y. Tsymbal, Spin-neutral currents for spintronics, Nat. Commun. **12**, 7061 (2021).

[24] K. Koepernik, M. D. Johannes, R. González-Hernández, and L. Šmejkal, Prediction of unconventional magnetism in doped $FeSb_2$, PNAS **118**, e2108924118 (2021).

[25] Z. Feng, X. Zhou, L. Šmejkal, L. Wu, Z. Zhu, H. Guo, R. González-Hernández, X. Wang, H. Yan, P. Qin, and X. Zhang, An anomalous Hall effect in altermagnetic ruthenium dioxide, Nat. Electron. **5**, 735 (2022).

[26] K. Kim, J. Lee, J. Lee, S. Han, and J. Kang, Formation and characterization of manganese silicide on Si(111) and Si(100) substrates, J. Korean Phys. Soc. **51**, 1032 (2007).

[27] A. Allam, P. Boulet, and M.-C. Record, Phase formation in Mn–Si thin films during rapid thermal annealing, Intermetallics **37**, 69 (2013).

[28] L. Zhang and D. G. Ivey, Low temperature reactions of thin layers of Mn with Si, J. Mater. Res. **6**, 1518 (1991).

[29] M. Trabel, N. V. Tarakina, C. Pohl, J. Constantino, C. Gould, K. Brunner, and L. Molenkamp, Twin domains in epitaxial thin MnSi layers on Si(111), J. Appl. Phys. **121**, 245310 (2017).

[30] E. Karhu, S. Kahwaji, M. Robertson, H. Fritzsche, B. J. Kirby, C. F. Majkrzak, and T. Monchesky, Helical magnetic order in MnSi thin films, Phys. Rev. B **84**, 060404(R) (2011).

[31] S. Higashi, P. Kocán, and H. Tochihara, Reactive epitaxial growth of MnSi ultrathin films on Si(111) by Mn deposition, Phys. Rev. B **79**, 205312 (2009).

[32] T. Suzuki, T. Lutz, B. Geisler, P. Kratzer, K. Kern, and G. Costantini, Surface morphology of MnSi thin films grown on Si(111), Surf. Sci. **617**, 106 (2013).

[33] E. Magnano, E. Carleschi, A. Nicolaou, T. Pardini, M. Zangrando, and F. Parmigiani, Growth of manganese silicide films by co-deposition of Mn and Si on Si(111): A spectroscopic and morphological investigation, Surf. Sci. **600**, 3932 (2006).

[34] S. Azatyan, O. Utas, N. Denisov, A. Zotov, and A. Saranin, Variable termination of MnSi/Si(111)$\sqrt{3} \times \sqrt{3}$ films and its effect on surface properties, Surf. Sci. **605**, 289 (2011).

[35] M. Petit, L. Michez, C.-E. Dutoit, S. Bertaina, V. Dolocan, V. Heresanu, M. Stoffel, and V. Le Thanh, Very low-temperature epitaxial growth of Mn_5Ge_3 and $Mn_5Ge_3C_{0.2}$ films on Ge(111)

using molecular beam epitaxy, Thin Solid Films **589**, 427 (2015).

[36] S. Olive-Mendez, A. Spiesser, L. Michez, V. Le Thanh, A. Glachant, J. Derrien, T. Devillers, A. Barski, and M. Jamet, Epitaxial growth of Mn_5Ge_3/Ge(111) heterostructures for spin injection, Thin Solid Films **517**, 191 (2008).

[37] A. Ishizaka and Y. Shiraki, Low temperature surface cleaning of silicon and its application to silicon mbe, J. Electrochem. Soc. **133**, 666 (1986).

[38] R. Schlitz, P. Swekis, A. Markou, H. Reichlova, M. Lammel, J. Gayles, A. Thomas, K. Nielsch, C. Felser, and S. T. Goennenwein, All electrical access to topological transport features in $Mn_{1.8}$PtSn films, Nano Lett. **19**, 2366 (2019).

[39] B. Aronsson, A note on the compositions and crystal structures of Mnb_2 Mn_3Si Mn_5Si_3 and $FeSi_2$, Acta Chem. Scand. **14**, 1414 (1960).

[40] B. Boren, Roentgenuntersuchung der Legierungen von Silicium mit Chrom, Mangan, Kobalt und Nickel, Z. fur Metall. **48**, 126 (1957).

[41] A. I. Figueroa, S. L. Zhang, A. A. Baker, R. Chalasani, A. Kohn, S. C. Speller, D. Gianolio, C. Pfleiderer, G. van der Laan, and T. Hesjedal, Strain in epitaxial MnSi films on Si(111) in the thick film limit studied by polarization-dependent extended x-ray absorption fine structure, Phys. Rev. B **94**, 174107 (2016).

[42] B. Geisler, P. Kratzer, T. Suzuki, T. Lutz, G. Costantini, and K. Kern, Growth mode and atomic structure of MnSi thin films on Si(111), Phys. Rev. B **86**, 115428 (2012).

[43] D. Morikawa, Y. Yamasaki, N. Kanazawa, T. Yokouchi, Y. Tokura, and T.-h. Arima, Determination of crystallographic chirality of MnSi thin film grown on Si(111) substrate, Phys. Rev. Mater. **4**, 014407 (2020).

[44] B. D. Cullity, *Elements of X-ray Diffraction: Pearson New* (Addison-Wesley Publishing, Boston, MA, 1956).

[45] S. Hasegawa, Reflection high-energy electron diffraction, Charact. Mater. **97**, 1925 (2012).

[46] M. Petit, A. Boussadi, V. Heresanu, A. Ranguis, and L. Michez, Step flow growth of Mn_5Ge_3 films on Ge(111) at room temperature, Appl. Surf. Sci. **480**, 529 (2019).

[47] E. Karhu, S. Kahwaji, T. L. Monchesky, C. Parsons, M. D. Robertson, and C. Maunders, Structure and magnetic properties of MnSi epitaxial thin films, Phys. Rev. B **82**, 184417 (2010).

[48] R. M. Walser and R. W. Bené, First phase nucleation in silicon-transition-metal planar interfaces, Appl. Phys. Lett. **28**, 624 (1976).

[49] M. Ronay, Reinvestigation of first phase nucleation in planar metal-Si reaction couples, Appl. Phys. Lett. **42**, 577 (1983).

[50] R. Pretorius, T. K. Marais, and C. C. Theron, Thin film compound phase formation sequence: An effective heat of formation model, Mater. Sci. Rep. **10**, 1 (1993).

[51] H. Okamoto, Mn-Si (Manganese-Silicon), J. Phase Equilib. **12**, 505 (1991).

[52] A. Berche, J. C. Tédenac, and P. Jund, First-principles determination of the enthalpy of formation of Mn-Si phases, Solid State Commun. **188**, 49 (2014).

[53] A. Kumar, M. Tallarida, M. Hansmann, U. Starke, and K. Horn, Thin manganese films on Si(111)-(7 × 7): Electronic structure and strain in silicide formation, J. Phys. D **37**, 1083 (2004).

[54] K. Schwinge, C. Müller, A. Mogilatenko, J. Paggel, and P. Fumagalli, Structure and magneto-optic kerr measurements of epitaxial MnSi films on Si(111), J. Appl. Phys. **97**, 103913 (2005).

[55] J. H. Grytzelius, H. M. Zhang, and L. S. O. Johansson, Coverage dependence and surface atomic structure of Mn/Si(111)-$\sqrt{3} \times \sqrt{3}$ studied by scanning tunneling microscopy and spectroscopy, Phys. Rev. B **80**, 235324 (2009).

[56] M. Eizenberg and K.-N. Tu, Formation and Schottky behavior of manganese silicides on n-type silicon, J. Appl. Phys. **53**, 6885 (1982).

[57] F. d'Heurle and P. Gas, Kinetics of formation of silicides: A review, J. Mater. Res. **1**, 205 (1986).

[58] R. Bene, A kinetic model for solid-state silicide nucleation, J. Appl. Phys. **61**, 1826 (1987).

[59] U. Gösele and K.-N. Tu, "Critical thickness" of amorphous phase formation in binary diffusion couples, J. Appl. Phys. **66**, 2619 (1989).

[60] W. Meng, B. Fultz, E. Ma, and W. Johnson, Solid-state interdiffusion reactions in Ni/Ti and Ni/Zr multilayered thin films, Appl. Phys. Lett. **51**, 661 (1987).

[61] G. Ctistis, U. Deffke, K. Schwinge, J. J. Paggel, and P. Fumagalli, Growth of thin Mn films on Si(111)-7 × 7 and Si(111)-$\sqrt{3} \times \sqrt{3}$: Bi, Phys. Rev. B **71**, 035431 (2005).

[62] W. Meng, C. Nieh, and W. Johnson, Maximum thickness of amorphous NiZr interlayers formed by a solid-state reaction technique, Appl. Phys. Lett. **51**, 1693 (1987).

[63] M. Hortamani, P. Kratzer, and M. Scheffler, Density-functional study of Mn monosilicide on the Si(111) surface: Film formation versus island nucleation, Phys. Rev. B **76**, 235426 (2007).

[64] G. Ottaviani, Metallurgical aspects of the formation of silicides, Thin Solid Films **140**, 3 (1986).

[65] C. Pfleiderer, P. Böni, T. Keller, U. Rößler, and A. Rosch, Non-Fermi liquid metal without quantum criticality, Science **316**, 1871 (2007).

[66] W.-Y. Choi, H.-W. Bang, S.-H. Chun, S. Lee, and M.-H. Jung, Skyrmion phase in MnSi thin films grown on sapphire by a conventional sputtering, Nanoscale Res. Lett. **16**, 7 (2021).

[67] E. Magnano, F. Bondino, C. Cepek, F. Parmigiani, and M. Mozzati, Ferromagnetic and ordered MnSi(111) epitaxial layers, Appl. Phys. Lett. **96**, 152503 (2010).

[68] S. Zhang, R. Chalasani, A. Baker, N.-J. Steinke, A. Figueroa, A. Kohn, G. van der Laan, and T. Hesjedal, Engineering helimagnetism in MnSi thin films, AIP Adv. **6**, 015217 (2016).

[69] N. Biniskos, K. Schmalzl, S. Raymond, S. Petit, P. Steffens, J. Persson, and T. Brückel, Spin Fluctuations Drive the Inverse Magnetocaloric Effect in Mn_5Si_3, Phys. Rev. Lett. **120**, 257205 (2018).

[70] L. Vinokurova, V. Ivanov, E. Kulatov, and A. Vlasov, Magnetic phase transitions and electronic structure of the manganese silicides, J. Magn. Magn. Mater. **90**, 121 (1990).

[71] S. C. Das, K. Mandal, P. Dutta, S. Pramanick, and S. Chatterjee, Observation of inverted hysteresis loop and thermomagnetic irreversibility in the antiferromagnetic Mn_5Si_3 alloy, Phys. Rev. B **100**, 024409 (2019).

[72] M. Ait Haddouch, N. Abboushi, N. Sharma, A. Eich, A. Grzechnik, C. Li, M. Tolkiehn, H. Alsamamra, J. Voigt, and K. Friese, Site dependence of the magnetocaloric effect in $Mn_{5-x}Fe_xSi_3$, J. Appl. Crystallogr. **55**, 1164 (2022).